AD-A233 981

Pressure Distribution and Induced Force Field on a Conical Nozzle due to Impingement of a Normal Jet into the Supersonic Cross-Flow

Prepared by

F. BABAN, E. M. KAEGI, M. A. KWOK
R. L. VARWIG, and R. G. AURANDT
Aerophysics Laboratory
Laboratory Operations

15 February 1991

Prepared for

SPACE SYSTEMS DIVISION
AIR FORCE SYSTEMS COMMAND
Los Angeles Air Force Base
P. O. Box 92960
Los Angeles, CA 90009-2960
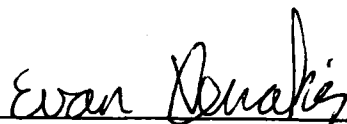
Engineering and Technology Group

THE AEROSPACE CORPORATION
El Segundo, California

This report has been reviewed by the Public Affairs Office (PAS) and is releasable to the National Technical Information Service (NTIS). At NTIS, it will be available to the general public, including foreign nationals.

This technical report has been reviewed and is approved for publication. Publication of this report does not constitute Air Force approval of the report's findings or conclusions. It is published only for the exchange and stimulation of ideas.

EVAN XENAKIS, Lt, USAF
MOIE Project Officer
SSD/MZSEB

JONATHAN M. EMMES, Maj, USAF
MOIE Program Manager
PL/WCO OL-AH

REPORT DOCUMENTATION PAGE

1a. REPORT SECURITY CLASSIFICATION Unclassified			1b. RESTRICTIVE MARKINGS		
2a. SECURITY CLASSIFICATION AUTHORITY			3. DISTRIBUTION/AVAILABILITY OF REPORT Approved for public release; distribution unlimited		
2b. DECLASSIFICATION/DOWNGRADING SCHEDULE					
4. PERFORMING ORGANIZATION REPORT NUMBER(S) TR-0090(5930-01)-2			5. MONITORING ORGANIZATION REPORT NUMBER(S) SSD-TR-91-05		
6a. NAME OF PERFORMING ORGANIZATION The Aerospace Corporation Laboratory Operations		6b. OFFICE SYMBOL (If applicable)	7a. NAME OF MONITORING ORGANIZATION Space Systems Division		
6c. ADDRESS (City, State, and ZIP Code) El Segundo, CA 90245-4691			7b. ADDRESS (City, State, and ZIP Code) Los Angeles Air Force Base Los Angeles, CA 90009-2960		
8a. NAME OF FUNDING/SPONSORING ORGANIZATION		8b. OFFICE SYMBOL (If applicable)	9. PROCUREMENT INSTRUMENT IDENTIFICATION NUMBER F04701-88-C-0089		
8c. ADDRESS (City, State, and ZIP Code)			10. SOURCE OF FUNDING NUMBERS		

			PROGRAM ELEMENT NO.	PROJECT NO.	TASK NO.	WORK UNIT ACCESSION NO.

11. TITLE *(Include Security Classification)*
Pressure Distribution and Induced Force Field on a Conical Nozzle due to Impingement of a Normal Jet into the Supersonic Cross-Flow

12. PERSONAL AUTHOR(S)
Baban, Farzad; Kaegi, Emil M.; Kwok, Munson A.; Varwig, Robert L.; and Aurandt, Richard G.

13a. TYPE OF REPORT	13b. TIME COVERED FROM _____ TO _____	14. DATE OF REPORT (Year, Month, Day) 1991 February 15	15. PAGE COUNT 32

16. SUPPLEMENTARY NOTATION

17.	COSATI CODES		18. SUBJECT TERMS *(Continue on reverse if necessary and identify by block number)* Liquid/Gaseous Transverse Injection Supersonic Nozzle Flow Thrust Vector Control
FIELD	GROUP	SUB-GROUP	

19. ABSTRACT *(Continue on reverse if necessary and identify by block number)*

An experimental investigation was undertaken to study the pressure distributions and the induced side force on the wall of a conical nozzle due to intrusion of a jet into a supersonic cross-flow. The experiment was carried out to simulate the side injection of fuel coolant from the regenerative cooling system into the supersonic exhaust gas discharging through the nozzle of a rocket engine. The motivation was to shed light on an engine anomaly that occurred during the first Titan IV launch, and thereby to reject or to substantiate the hypothesis that two or three ruptured regenerative cooling tubes caused the near-normal injection of liquid fuel (Aerozine-50) into the exhaust gas in the expansion nozzle section. This scenario was the prime reason for one of the engines to gimbal over to its extreme stop position.

The flow of nitrogen (700 psi plenum pressure) through a 1/30th subscale converging-diverging nozzle simulated the exhaust (main) flow. Injection of a liquid (Freon-11, water) or a gas (nitrogen) from an injection port drilled at the most probable wall location provided the penetrating side jet. Mass flow rate ratios (jet-to-main flow rates), as well as local Mach number, were matched as closely as possible with those reported from the actual flight data. The mass flow ratio was varied to assess the sensitivity of the results to the relative momentum of the jet. Later, wires with different aspect ratios were situated in the supersonic stream replacing the impinging jet at the location of injection. This was done to compare the flow field around a solid bluff body with that around an impinging liquid jet. The induced force field on the interior nozzle wall and the location of the center of force for both liquid and gaseous impinging jets were compared with one another and against the results obtained for the bluff body case. The flow phenomena for these different cases are presented in this report.

20. DISTRIBUTION/AVAILABILITY OF ABSTRACT ☐ UNCLASSIFIED/UNLIMITED ☒ SAME AS RPT ☐ DTIC USERS		21. ABSTRACT SECURITY CLASSIFICATION Unclassified	
22a. NAME OF RESPONSIBLE INDIVIDUAL		22b. TELEPHONE (Include Area Code)	22c. OFFICE SYMBOL

PREFACE

CONTENTS

FIGURES

TABLES

I. INTRODUCTION

During the successful first Titan IV launch, one of the two liquid rocket engines on the improved Titan core vehicle gimballed over to its extreme stop position. Compensating thrust from the other liquid rocket engine permitted the planned flight trajectory to be completed. In order to investigate the underlying cause of this anomaly, a program team rapidly limited the possible scenarios to one or two.

The final scenario proposed by the team suggested that failure may have occurred in the regenerative cooling system located in the bell or expansion section of the liquid rocket nozzle downstream from the throat. By using telemetry data to bound the forces and moments required to overcome gimbal control action, analysts estimated that the force required could be caused by the thrust from lateral injection of liquid fuel coolant into the nozzle through a small hole in the nozzle wall. The side jet flow rate needed to push the gimbal to the stops depended on the moment arm. The center of force was estimated to be somewhere in the nozzle bell or the downstream skirt region.

Injection of a gas or a liquid in a nearly orthogonal direction into a cross-stream has been the subject of thorough investigation since the late 1940s. Pioneer work in this area has been done by Ruggeri and Callaghan[1-4] in a series of publications. Jordinson[5] was the first to experimentally determine that the cross section of an initially cylindrical jet is distorted by the shear flow into a horseshoe (kidney) shape. The investigations of Keffer and Baines,[6] Kamotani and Gerber[7] Chassaing et al.,[8] and Moussa et al.[9] shed more light on penetration height and trajectory of the jet, as well as the flow structures within the jet boundary. Holdman and Walker,[10] and Atkinson et al.[11] reported on mixing of a row of jets discharging into a cross-stream. All of the above investigations, however, dealt with jets penetrating into a subsonic cross-flow.

In the 1960s, injection of transverse jets into supersonic and hypersonic cross-streams became an important topic of investigation due to several technological applications. Of particular importance were the fields of external missile controls, rocket thrust vector control, control of hypersonic reentry vehicles, and fuel injection in the supersonic combustion ramjet (Scramjet). Since then, numerous investigators have been addressing fundamental issues in both liquid and gaseous transverse jets penetrating into supersonic cross-streams. References 12 through 25 are a few of the many investigations on this topic, some of which discuss the case of a sonic gaseous jet and some of which deal with the injection of a liquid into a supersonic cross-stream. In either case, the flow field is far more complicated than injection of a transverse jet into a subsonic cross-stream. The situation becomes even more complex for an expanding supersonic cross-stream where flow is not maintained at the same free stream Mach number.

The transverse injection of a gas or a liquid into a turbulent, axisymmetric mainstream forms a complex three-dimensional flow structure in the vicinity of the injection and immediately downstream, destroying the axisymmetry and thus inhibiting the easy application of well-established computational fluid dynamic codes for predicting the flow field. In simple terms, the injected fluid presents an obstruction to the main supersonic stream, which is compressed

7

through a shock wave as it turns to negotiate the obstruction. The shape and extent of the bow shock are determined by the trajectory and penetration of the jet which, in turn, are principally dependent on the jet-to-free stream momentum ratio and on whether the jet is liquid or gaseous. The jet momentum flux is related to the total pressure of the jet. However, one should keep in mind that the jet emerges into a complicated pressure field, and the relation of its static pressure to pressure in the surroundings will determine whether it is on-design, under-expanded, or over-expanded. The strong interaction shock causes the boundary layer to separate. The boundary layer might be either laminar or turbulent, resulting in different degrees of separation and a separation shock that attaches itself to the interaction bow shock. The distinct, separate vortices of counter-rotating flow are formed upstream of the jet, extending several jet diameters into the separated region where fairly low momentum flow exists. Figure 1 shows a general description of the flow field about a liquid (1a) and a gaseous (1b) jet on a symmetry plane of injection, impinging orthogonally to a supersonic gas stream. Despite the obvious similarities, some fundamental differences can be observed. For the case of a liquid injection, the jet remains collimated after leaving the injector for a distance of 4 to 5 diameters. At greater distances, the jet cross section becomes distorted, and instabilities rapidly disintegrate the jet into a number of large liquid structures, the mean size of which is a function of the initial jet diameter. By the time the jet reaches a height of approximately two-thirds the penetration height, it has completely disintegrated. The resulting droplets follow individual trajectories, since the distance between droplets is large. Needless to say, the liquid injection case generates a two-phase flow condition. In the simplest case, aerosol droplets will be transported in the gaseous freestream. In the usual case, as with rocket fuels, evaporation of droplets, and even recondensation and precipitation, may become important further downstream.

Prior to the breakup and atomization process, when the jet is still collimated, a thin external boundary layer, formed from the gaseous-free stream flow interacting with the liquid injectant, is enveloping the jet. As a defined structured jet, this flow may persist for several exit diameters (10 to even 100).[19] In this portion, the mainstream flow "sees" the jet more or less like a solid bluff body. In fact, some investigators have alluded to the correlation between liquid jet breakup and the Strouhal number associated with vortices shed past a circular or elliptical surface. This observation implies a relationship between transverse liquid jet breakup and the generation of vorticity at the liquid-gas interface, which can result in the formation of vortical structures within the liquid jet and the characteristic kidney-shaped cross section.

For the gaseous injection case, the mainstream is once again obstructed by the transverse jet, and a relatively strong interaction bow shock is developed upstream of the injection. Flow is separated upstream of the jet, and at least two counter-rotating vortical structures are present in this region. Analogous to injection of a liquid into a cross-stream, the gaseous jet entering the main flow is curved because of the centripetal force caused by the pressure difference between the leading edge and the rear of the jet. The leading edge pressure is increased by the retarding effect of the jet on the primary flow, while the rarefaction that occurs at the rear causes a decrease in pressure. Unlike the liquid jet injection, the highly under-expanded gaseous jet rapidly expands to match pressures at its boundaries with the low-pressure surroundings. The supersonic injectant flow then turns downstream, creating a recompression region and leading to a structure

8

(a)

(b)
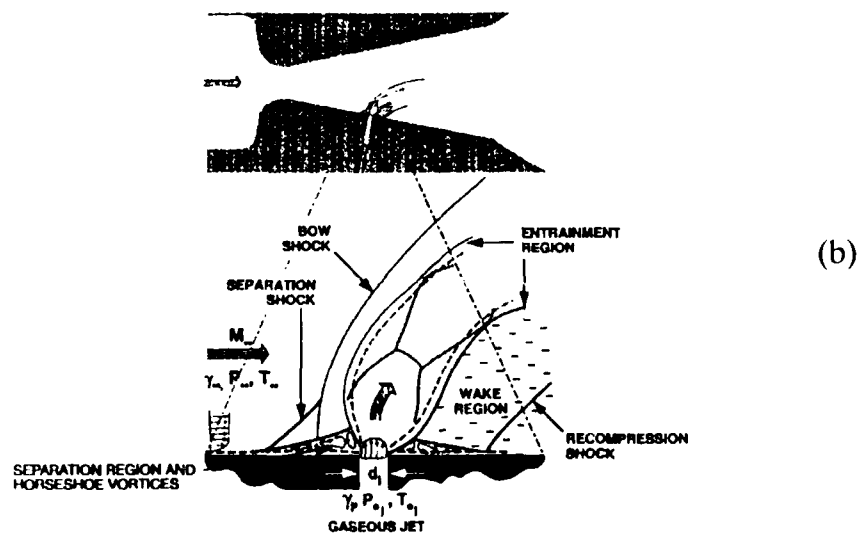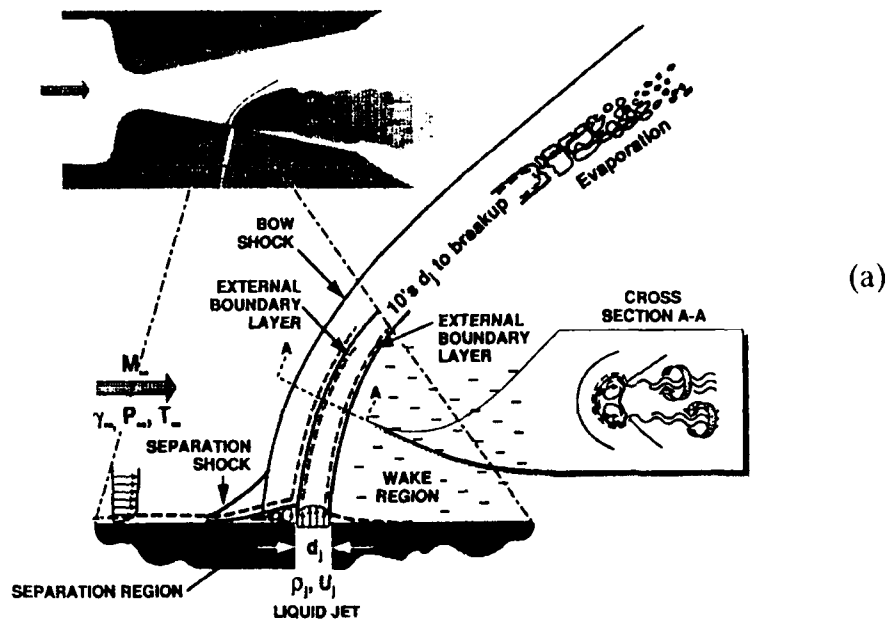
Fig. 1. Schematic of the Flow Field in the Vicinity of a Transverse Jet
Impinging into a Supersonic Cross-Stream. (a) Liquid jet; (b) gaseous
jet.

requiring a strong, nearly normal shock at the location of the Mach disc, through which the central core of the jet passes. Obviously, for the case of a gaseous jet impinging into a gaseous cross-stream, no two-phase flow regions exist, and the jet does not undergo the same breakup process as in the liquid injection case. However, multiple species flow may have to be considered since the free stream and injectant gases may be different. Another significant difference with gaseous jets would be the rapid degree of entrainment and mixing that can occur. Structurally, penetration will not be as great (order of 10 exit diameters), and this behavior will have a major effect on downstream wake configurations and consequent wall pressure distributions.

In what follows, the pressure distributions and the induced side force due to impingement of a liquid jet issuing into a supersonic nozzle flow are reported. The location of the center of force relative to the injection port is also obtained. The results for the liquid case pertain to injection of Freon-11, as well as water, into a supersonic cross-stream of gaseous nitrogen. These results are compared with those obtained for gaseous nitrogen being injected normally into the same supersonic cross-flow. Sensitivity of the results to the mass flow ratio (jet-to-main flow) are assessed by varying the injection plenum pressure. Furthermore, the results obtained for a wire replacing the fluid injection at the location of injection are presented in this report. This is done to examine the case of an infinitely stiff jet penetrating into the cross-flow. Finally, the results of a flow visualization technique using thin oil film dots painted on the interior surface of the nozzle will be reported.

II. EXPERIMENTAL PROGRAM

In order to verify the hypothesis and to eliminate competing Titan IV anomaly scenarios, a cold flow subscale experiment was designed to assess the gas dynamic effects due to intrusion of a lateral fluid jet into an axisymmetric, supersonic nozzle flow. An approximately 1/30th scale converging-diverging conical nozzle with 16:1 expansion ratio was used to simulate the actual liquid rocket flow. The test model was made of a 5-in.-long stainless steel solid cylinder, the inside of which was machined to produce a converging-diverging conical nozzle. The nozzle had a 0.5-in.-diameter throat and a 14° half angle conical expansion section. The length of the nozzle from the throat to the exit measured 3 in. (Fig. 2). An array of static pressure taps was drilled in both the azimuthal and axial directions to allow the local static pressure to be measured on the nozzle wall. The taps were drilled 1/4 in. apart in the stream direction and 12° apart in the azimuthal direction. In order to minimize the number of required pressure taps and pressure transducers, not one, but an array of small holes was drilled to serve as injection ports. The holes were drilled at the most probable scaled-down location where an actual hole might have occurred during flight. Based on the actual flight data, the center of the hole created during the Titan IV flight was estimated to be near the end of the regeneratively cooled nozzle section and the beginning of the aft nozzle skirt. This corresponds to the expansion ratio of nearly 6:1 in the actual nozzle. However, it should be noted that there are some differences between the actual nozzle and the prototype model used in this experiment.

The expansion section of the actual nozzle was contoured, and its exit-to-throat area ratio was 15:1. Considering these differences, the location of the injection ports was chosen so that the estimated free-stream Mach number of the real flow would be matched at the location of injection. This corresponded to the station where the expansion ratio was about 5.2 on the test model. At this location, several injection ports were made 12° apart from one another in the azimuthal direction (Fig. 2). The injection ports were drilled in the vicinity of the pressure taps. By injecting the injectant through one of these ports at a time, in a repetitive sequence of experiments with the same flow conditions, temporal pressure data at each station were acquired. In so doing, the domain of measurements extended from 0 to 72° in the azimuthal direction and from the injection port down to the exit plane in the axial direction. Figure 3 shows the map of the domain of measurements projected onto the X-Z plane.

In addition to the measurement points shown in this figure, an array of pressure taps was drilled directly opposing the existing one so that the flow symmetry or asymmetry could be verified. The measurements of local static pressure were made possible by using eight Endevco pressure transducers, model 8510, with different ranges and sensitivities. Two of the transducers with 0 to 2000 psi range were used to measure the main plenum pressure and the injection plenum pressure. The remaining six transducers were more sensitive and had different ranges (0 to 15, 0 to 50, and 0 to 100 psi). These transducers were inserted in the pressure taps near the injection ports and provided the temporal pressure data at the locations shown in Fig. 3. The signal obtained from each transducer was amplified by an Analog Devices signal conditioner, model 3B18, before being fed through an analog-to-digital data acquisition board. The gain on each
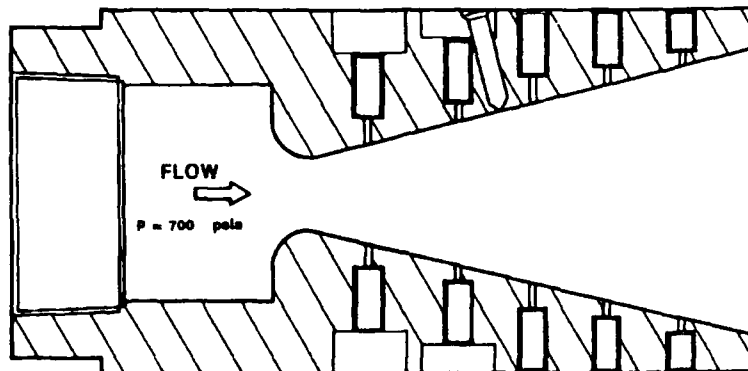
- 1/30th−SCALE MODEL
- 16:1 EXPANSION RATIO
- 33 PRESSURE TAPS IN THE VICINITY AND DOWNSTREAM OF INJECTION PORT
- PRESSURE TAPS ON THE OPPOSITE SIDE FOR SYMMETRIC CHECK
- 6 INJECTION PORTS 12° APART A/A* = 5.23

Fig. 2. Test Model Showing Some of the Pressure Taps and the Injection Port on the Expansion Section of the Converging-Diverging Nozzle
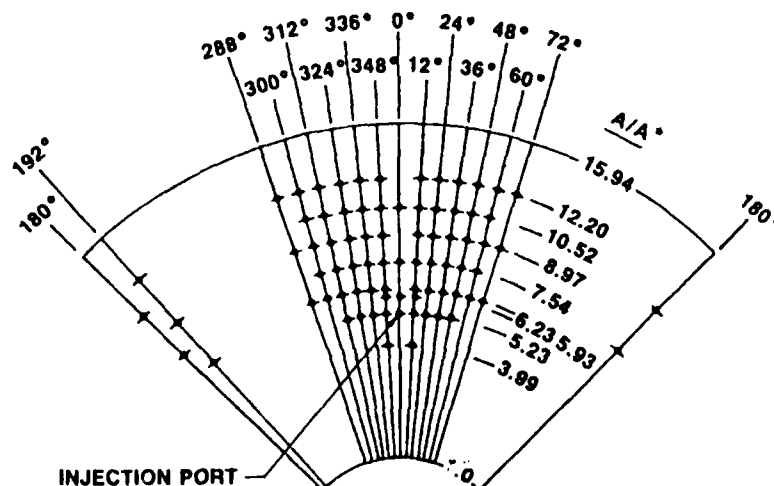

Fig. 3. Domain of Pressure Measurements Mapped onto a Plane

12

amplifier was set by considering the excitation voltage and the sensitivity of the given transducer and the saturation limit of the A/D board. Factory supplied calibration factors were used.

In addition to matching the Mach number, the simulation approximately matched the very high pressures of the mainstream flow and the coolant plenum. The subscaled mass flows were chosen so that the ratio of injectant flow rate to nozzle flow rate would range over the values estimated for the actual nozzle flow. The subscale flow exhausted into a vacuum tank to simulate the low background pressures of the upper atmosphere. Under these defined constraints, the experimental objectives were to study the structure of the flow, to verify the projected ratios of side force-to-nozzle thrust, to document nozzle moments, and to determine the sensitivity of side force centroid locations to varied flow conditions.

The mainstream flow was gaseous nitrogen supplied from a 7.2 cu. ft. capacity, portable gas storage system. The system was pressurized to approximately 800 psi from bottled nitrogen. The flow was controlled through ASCO solenoid valves and a timing network. Duration of the mainstream flow was set for 1 second.

Freon-11 (CCl_3F) was chosen as a primary injectant. It is a high molecular weight liquid injectant which could turn to an aerosol and then to vapor under the test conditions. This physical behavior would be similar to that of the actual Aerozine-50 coolant (50% N_2H_4, 50% UDMH) before chemical reaction in the mainstream (Fig. 3). In addition to Freon, water was used as a liquid fuel surrogate, and nitrogen was used as a reference case of a gaseous injectant. Both liquid injectants (Freon and water) were pressurized to approximately 700 psi by means of a pressurized nitrogen bottle before being injected into the mainstream. Two ASCO solenoid valves were mounted immediately before and after the liquid injectant container to regulate the duration of injection. The injection valves were triggered with 0.5 second delay relative to the mainstream flow and remained open for a duration of 0.3 second. The flow rate of the liquid injectant was obtained by accurately measuring the volume of liquid in the container before and after the injection and keeping record of the time during which the injection solenoid valves were open.

One-dimensional flow analyses were carried out to estimate the free-stream condition at the station of injection (i.e., $A/A^* = 5.23$). For a nominal pressure of 700 psi in the mainstream nitrogen plenum, Mach number, Reynolds number, and pressure at the injection station were estimated to be 3.2, 9.4×10^6, and 13.7 psi, respectively. The boundary layer thickness was found to be nearly 4.0×10^{-4} in. at $A/A^* = 5.23$. With the thin layer, even for the small size test model used in this experiment, it is quite reasonable to disregard the boundary layer and assume a free-stream flow throughout any unperturbed cross section.

Later, a thin copper wire whose outer diameter nearly matched the inner diameter of the injection hole was introduced into the supersonic cross-flow. The wire was placed normal to the nozzle wall and protruded 6.35 mm into the flow. This gave a 12.5 aspect ratio for the exposed wire. The sensitivity of the results to the aspect ratio of the wire was examined by placing a jacket (wire insulation) on the wire. In so doing, the aspect ratio of the wire was reduced by a factor of 2 (i.e., $h/d = 6.25$).

In order to obtain a better understanding of the physics of the flow, an attempt was also made to visualize the flow. Since the flow discharged into a vacuum chamber rather than the

atmosphere, a real-time visualization technique was not attempted. However, an oil-smearing technique was used to track the footprint of the bow shock created from the intrusion of the jet into the mainstream supersonic flow. This was done by painting a thin dark oil film on the conical interior of the nozzle. The model was first disassembled, and oil film in the form of small dots was painted on the nozzle wall. The model was then carefully remounted on the test rig making sure that the oil dots were not smeared. The test was run, and the model was then dismounted for postmortem examination. Several trial runs were performed to gain experience on how far apart the oil dots should be and how thick a film was needed to obtain a clear picture.

III. DATA ACQUISITION, PROCESSING, AND ANALYSIS

The output signal from each pressure transducer was fed through a signal conditioner before being digitized by a 12-bit Metrabyte Dash-8 analog-to-digital converter. This board is capable of digitizing eight signals. Thus, eight pressure transducers connected to eight signal conditioners used the full capability of the board and minimized the number of runs required to map the entire domain of measurements. The digitized signals were then stored on an IBM personal computer operating under Labtech Notebook software and were subsequently transferred to a digital MicroVAX II for postprocessing (see Fig. 4 for the block diagram). Data were collected at a fixed rate of 400 samples per second for a record length of 2 seconds. The main flow was triggered approximately 0.2 second after data collection had begun so that the dc offset at each channel could be obtained. The main flow was maintained for a duration of 1 second. In so doing, the local static pressure before, during, and after the injection was obtained. This provided a good means for comparison between the base local static pressure (i.e., no injection) and the local static pressure during injection. The analog signals from the signal conditioners were monitored by several Tektronix oscilloscopes. Since no time series analyses were to be performed on the digitized data, no attempt was made to filter the signal below the Nyquist frequency. Needless to say, this introduced an aliasing error in the analysis of the digitized data. The quantization error was estimated to have a uniform probability distribution with a standard deviation of approximately 0.29 scale unit.[26] Since a 12-bit analog-to-digital converter was used, a peak signal-to-noise ratio of 80 dB (10^4 in amplitude) was obtained. Thus, the quantization error was negligible relative to other experimental sources of error.

Analysis on the digitized data was done by first subtracting the dc offset and then normalizing by the plenum pressure at the same instant. This eliminated the effect of pressure decrease in the plenum during each run (~5%) as a result of gas depletion in a finite-size reservoir.
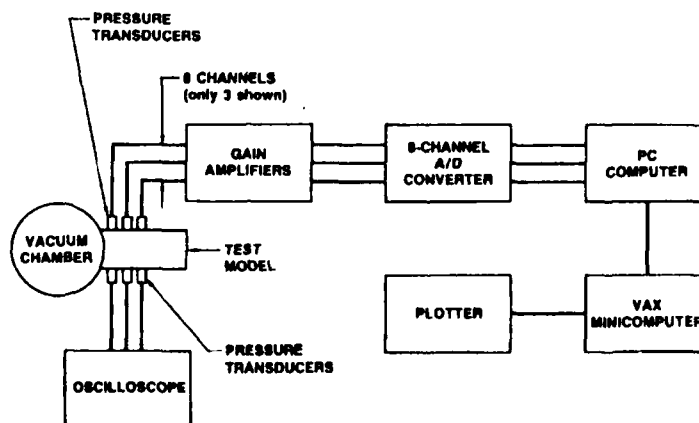
Fig. 4. Block Diagram of the Instrumentation and Data Acquisition

15

A. SIDE FORCE ANALYSIS

The normalized pressure before the injection was subtracted from the normalized pressure during injection to obtain the change in pressure due to impingement of the side jet into the main nozzle flow. The resultant side force induced on the nozzle wall was computed by integrating this pressure difference over the domain of the measurements. This was done by multiplying the pressure difference measured at every point by the elemental surface area surrounding the point of measurement. To obtain an expression for the elemental surface areas, the expression for the entire surface area of a cone is obtained in terms of the cone half angle (α) and its height (H).

Surface area of a surface of revolution is given by

$$\text{Surface Area} = S = \int_{\theta_1}^{\theta_2} \int_{x=a}^{b} f(x)\sqrt{1 + [f'(x)]^2} \; dx d\theta \tag{1}$$

where $f(x)$ for $a \leq x \leq b$ is a non-negative curve rotated about the x-axis to generate the surface. $f'(x)$ must be continuous for $a \leq x \leq b$.

For a cone, $f(x)$ is a straight line described by

$$f(x) = (\tan\alpha) \cdot x \tag{2}$$

and

$$f'(x) = \tan\alpha \tag{3}$$

Thus, for a cone of height H, the surface area is

$$S = 2\pi \int_{o}^{H} (\tan\alpha) \cdot x \sqrt{1 + \tan^2\alpha} \; dx \tag{4}$$

or

$$S = \pi \frac{\tan\alpha}{\cos\alpha} H^2 \tag{5}$$

Now, let us compute the elemental surface area bounded by $\Delta\Theta$ and Δx, where $\Delta\Theta$ is the measurement resolution in the azimuthal direction and Δx is the resolution of measurements in the axial direction. That is

$$\Delta\theta = \theta_2 - \theta_1, \text{ where } \theta_1 \leq \theta \leq \theta_2 \text{ and}$$

$$\Delta X = X_2 - X_1, \text{ where } X_1 \leq X \leq X_2.$$

Then, surface area is

$$S = \frac{\Delta\theta}{2} \frac{\tan\alpha}{\cos\alpha} \left(X_2^2 - X_1^2\right) \tag{6}$$

noting that $X_2 + X_1 = 2X$, Eq. (6) can be written as

$$S = \frac{\Delta\theta}{2} \frac{\tan\alpha}{\cos\alpha} (\Delta X)(2X) \tag{7}$$

For the present measurements:

$$\alpha = 14^\circ, \quad \Delta\theta = 12^\circ = \frac{\pi}{15}, \quad \Delta X = 0.25 \text{ in.}$$

Hence,

$$S = \frac{\pi}{60} \frac{\tan(14^\circ)}{\cos(14^\circ)} X \tag{8}$$

Therefore, the elemental surface area is conveniently expressed as a function of X (the location of pressure measurement relative to the vertex of the cone). Now, the magnitude of the force exerted at a particular measured point can be obtained by multiplying the measured pressure difference, P_i, by its own respective elemental surface area, S_i. However, to obtain the resultant side force exerted on the cone in the y-direction, each individual force must first be projected onto the plane of injection and then be projected into the y-direction. In doing so, we obtain

$$\text{Side Force} = \frac{\pi}{60} \cdot \tan(\alpha) \cdot \left(2 \sum_{i=1}^{N} P_i X_i \cos\theta_i - \sum_{i=1}^{n} P_i X_i \cos\theta_i\right) \tag{9}$$

where N is the total number of measured points and n is the number of measured points along the generator that passes through the injection port ($\Theta = 0$ generator). Symmetry is assumed and incorporated in the above equation to obtain the total force on the nozzle wall. Note that in using the above equation in the presented form, X's must be in inches and P's must be in psi units so that the force is properly dimensional in lbf.

B. CENTER-OF-FORCE ANALYSIS

To obtain the location of center of force, the moment of individual forces with respect to a point (e.g., the vertex of the cone) must first be calculated.

Let us assume that the vectorial presentation of each individual force perpendicular to its own elemental surface is

$$\vec{F} = A \cdot \vec{i} + B \cdot \vec{j} + c \cdot \vec{k} \tag{10}$$

17

Then the vector $\vec{r}$ joining the vertex of the cone to the point of application of the force is the moment arm, and it can be expressed without loss of generality as

$$\vec{r} = x\,\vec{i} + x\tan\alpha\cos\theta\,\vec{j} + x\tan\alpha\sin\theta\,\vec{k} \tag{11}$$

$$\vec{u}_r = \cos\alpha\,\vec{i} + \sin\alpha\cos\theta\cdot\vec{j} + \sin\alpha\sin\theta\,\vec{k} \tag{12}$$

However, $\vec{F}$ is perpendicular to $\vec{U}_r$; hence,

$$\vec{u}_r \cdot \vec{F} = 0. \tag{13}$$

or

$$\cos\alpha A + \sin\alpha\cos\theta\,B + \sin\alpha\sin\theta\,C = O \tag{14}$$

The moment of $\vec{F}$ with respect to the vertex is a vector perpendicular to the plane containing $\vec{r}$ and $\vec{F}$. This plane, which will be called the Plane of Force application, can be conveniently expressed as

$$\tan\theta\,Y - Z = O \tag{15}$$

for $\vec{F}$ to be in this plane

$$C = \tan\theta\cdot B \tag{16}$$

Therefore, Eq. (14) can be rewritten

$$\cos\alpha\,A + \sin\alpha\cos\theta\,B + \tan\theta\sin\alpha\sin\theta\,B = O \tag{17}$$

$$\therefore A = -\frac{\tan\alpha}{\cos\theta}\,B \tag{18}$$

Hence, the vector in the direction of $\vec{F}$ is

$$-\frac{\tan\alpha}{\cos\theta}\,B\,\vec{i} + B\,\vec{j} + \tan\theta\,B\,\vec{K} \tag{19}$$

or

$$-\tan\alpha\,\vec{i} + \cos\theta\,\vec{j} + \sin\theta\,\vec{K} \tag{20}$$

The unit vector in this direction is

$$\vec{u}_F = -\sin\alpha\,\vec{i} + \cos\alpha\cos\theta\,\vec{j} + \cos\alpha\sin\theta\,\vec{K} \tag{21}$$

18

$$\therefore \vec{F} = F\left(-\sin\alpha\,\vec{i} + \cos\alpha\,\cos\theta\,\vec{j} + \cos\alpha\,\sin\theta\,\vec{K}\right) \qquad (22)$$

where F is the magnitude of $\vec{F}$ obtained by multiplying the measured pressure by its respective elemental surface area. Now, the moment of $\vec{F}$ with respect to the vertex can be calculated

$$\vec{m}_o = \vec{r} \times \vec{F} = \begin{vmatrix} \vec{i} & \vec{j} & \vec{K} \\ x & x\tan\alpha\,\cos\theta & x\tan\alpha\,\sin\theta \\ -F\sin\alpha & F\cos\alpha\,\cos\theta & F\cos\alpha\,\sin\theta \end{vmatrix} \qquad (23)$$

Simplifying Eq. (23) will give

$$\vec{m}_o = \frac{F \cdot X}{\cos\alpha}\left(-\sin\theta\,\vec{j} + \cos\theta\,\vec{K}\right) \qquad (24)$$

It is apparent from Eq. (24) that there will be no contribution of moment in the direction of $\vec{j}$ (y-direction) due to symmetry consideration. Thus, the effective magnitude of the moment is

$$m_o = \frac{\cos\theta}{\cos\alpha}\,F \cdot X \qquad (25)$$

Total resultant moment (M_o) can now be calculated by summing the individual moments (m_{oj}). Using the expression obtained for the resultant force, this will become

$$M_o = \frac{\pi}{60}\,\frac{\tan\alpha}{\cos^2\alpha}\left(2\sum_{i-1}^{N} P_iX_i{}^2\cos\theta_i - \sum_{i=1}^{n} p_iX_i^2\cos\theta_i\right) \qquad (26)$$

The location of center of force can now be found by dividing Eq. (26) by the resultant force in the direction perpendicular to $\vec{r}$ (direction of $\vec{F}$).

$$r_{c.f.} = \frac{1}{\cos\alpha}\,\frac{2\sum\limits_{i=1}^{N} P_iX_i^2\cos\theta_i - \sum\limits_{i=1}^{n} P_iX_i^2\cos\theta_i}{2\sum\limits_{i=1}^{N} P_iX_i\cos\theta_i - \sum\limits_{i=1}^{n} P_iX_i\cos\theta_i} \qquad (27)$$

The distance measured from the vertex along the nozzle axis (x-axis) is, therefore

$$X_{c.f.} = \frac{2\sum\limits_{i=1}^{N} P_iX_i^2\cos\theta_i - \sum\limits_{i=1}^{n} P_iX_i^2\cos\theta_i}{2\sum\limits_{i=1}^{N} P_iX_i\cos\theta_i - \sum\limits_{i=1}^{n} P_iX_i\cos\theta_i} \qquad (28)$$

19

C. AXIAL THRUST CALCULATION

The axial thrust developed through the nozzle was computed using the conventional thrust equation

$$\text{Thrust} = \lambda \left[\dot{m} V_e + (P_e - P_o) A_e \right] \tag{29}$$

where $\dot{m} V_e$ is the jet thrust (also called the gross thrust) and $(P_e - P_o) A_e$ is is the pressure thrust term. Here, the subscript "e" refers to the nozzle exit condition, while the subscript "o" denotes the plenum condition. λ is the divergence factor which accounts for reduction in axial thrust caused by the divergence of streamlines at the nozzle exit. For a conical nozzle, the flow in the divergence section can be assumed to be a source flow. Thus,

$$\lambda = \frac{1 + \cos \alpha}{2} \tag{30}$$

where α is the cone half-angle.

In terms of the measured quantities, the gross thrust term can be written as

$$\dot{m} V_e = \frac{\Gamma A^* P_o}{\sqrt{\gamma R T_o}} \tag{31}$$

or

$$\dot{m} V_e = \Gamma A^* \ P_o M_e \sqrt{T_e / T_o} \tag{32}$$

where A^* is the throat cross-sectional area and Γ is a function of the heat capacity ratio, γ, given by

$$\Gamma = \gamma \left(\frac{2}{\lambda + 1} \right)^{\frac{\gamma + 1}{2(\gamma - 1)}} \tag{33}$$

Also, T_e / T_o can be written in terms of the exit Mach number

$$T_e / T_o = \left(1 + \frac{\gamma - 1}{2} M_e^2 \right)^{-1} \tag{34}$$

Therefore

$$\dot{m} V_e = \Gamma A^* \ P_o M_e \left(1 + \frac{\gamma - 1}{2} M_e^2 \right)^{-1/2} \tag{35}$$

Substituting (35) into (24) would yield the expression for the axial thrust in terms of the known quantities

$$\text{Thrust} = \lambda \Gamma A^* P_o M_e \left(1 + \frac{\gamma - 1}{2} + M_e^2 \right)^{-1/2} + \lambda (P_e - P_o) A_e \qquad (36)$$

In all the foregoing analyses, attention must be brought to several points. First, to obtain the total induced side force, the component of the side force due to the momentum of the jet itself must be added to the resultant side force obtained from pressure asymmetry. Second, since no pressure taps could be placed in the immediate vicinity of the injection port, the very high shock recovery pressure in this region could only be estimated from the normal shock analysis. Third, throughout the analysis, symmetry is assumed with respect to the injection plane. This latter assumption was tested at several locations throughout the experiment, confirming the validity of this claim. Also, in computing the mass flow rate of the main flow and the gaseous injection, the value for the coefficient of discharge was assumed to be unity. The error introduced due to this assumption is believed to be negligible. Overlapping the locations of the pressure measurements during different tests ensured that the measurements were indeed repeatable. It was particularly important for the base flow to be repeatable, since the experiment was repeated a number of times in order to map the entire domain of measurements.

IV. RESULTS AND DISCUSSION

A typical trace of pressure in the plenum and the injection port is presented in Fig. 5, where Freon-11 (CCl_3F) was injected into the main flow of nitrogen. The duration of each flow (main and jet) and the delay between them, as well as the pressure decay due to gas depletion in a finite-size plenum, are depicted in this figure. As stated earlier, the effect of this decay ($\sim 5\%$) is deleted by normalizing the pressure with the plenum pressure at the same instant. Figure 6 is evidence in support of this claim, where the normalized pressure at various axial stations (A/A^*) along the $12°$ generator, measured azimuthally from the Freon injection port, is presented. Note that the pressure normalized in this way remains virtually a constant before the injection (base pressure) and changes significantly to a different constant value while the injection is on, subsequently dropping to the base pressure level as the injection is turned off. This figure also shows the general trend that change in pressure is more pronounced upstream and near the injection port. The pressure was quantified by averaging the pressure before the injection and subtracting it from the averaged pressure during the injection. Figure 7 shows this pressure difference in the domain of measurements where the height of each bar represents the magnitude of the pressure difference. The change in pressure from a measured location to the next measured point downstream is shown linear in a connect-the-points graphic. This was done to assist the reader in visualizing the pressure distribution trends and is not meant to portray detailed axial pressure dependences. In particular, the pressure increase from the base pressure to a high value across the shock would not be a linear increase. Despite this, we believe that this figure is more representative and illustrative of the pressure distribution than any contour plots of pressure we might synthesize, for example.

Integration of the pressure distribution, based on the analysis discussed earlier, yields the resultant side force induced on the nozzle wall due to pressure asymmetry. The side force (in the y-direction) was computed to be 5.073 lbf. The component of the side force generated due to the momentum of the intruding jet was calculated to be 1.539 lbf. Thus, the total resultant side force is 6.612 lbf, which amounts to 2.91% of the axial thrust (i.e., axial thrust = 227 lbf). The location of the center of force was computed to be 0.379 in. downstream from the injection port measured along the nozzle axis (Table 1).

To assess the sensitivity of the results to the mass flow ratio, Freon-11 was injected at a reduced plenum pressure. The results indicate that the ratio of side force to axial thrust and the location of the center of force do not change appreciably by reducing the injection mass flow rate by a factor of nearly 2. This illustrates that at least for these test conditions, results seem to be insensitive to mass-flow ratios, as long as gas sufficient fluid is injected to set up the shock interaction pattern. In much the same way, the pressure distribution in the vicinity and downstream of the injection port was obtained for water and then for nitrogen injection (Figs. 8 and 9, respectively). Comparing Fig. 7 with Fig. 8 clearly illustrates the similarity between the Freon-11 and water injections. Indeed, the side force generated as a result of pressure asymmetry created by water injection is calculated to be 5.386 lbf, which is nearly the same as that for Freon-11 injection. This
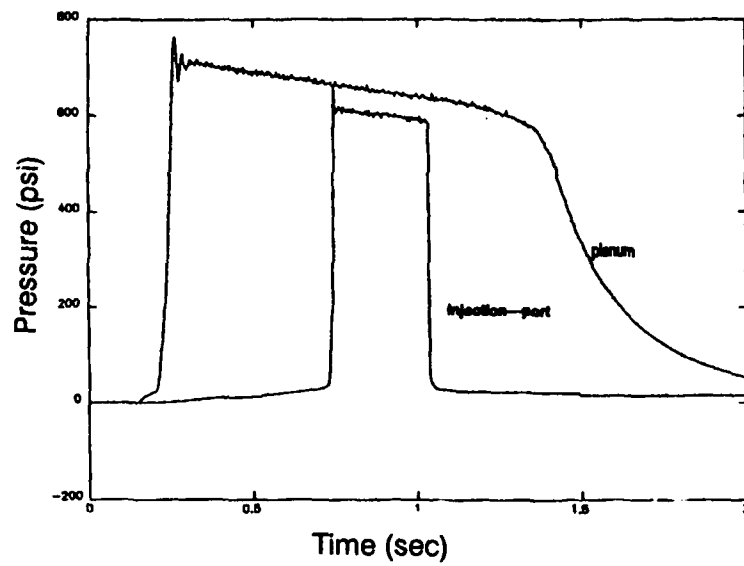
Fig. 5. The Reservoir Pressure for the 1-sec-Long Nitrogen Main-stream Flow and 0.2 sec Pulsed Freon-11 Injection
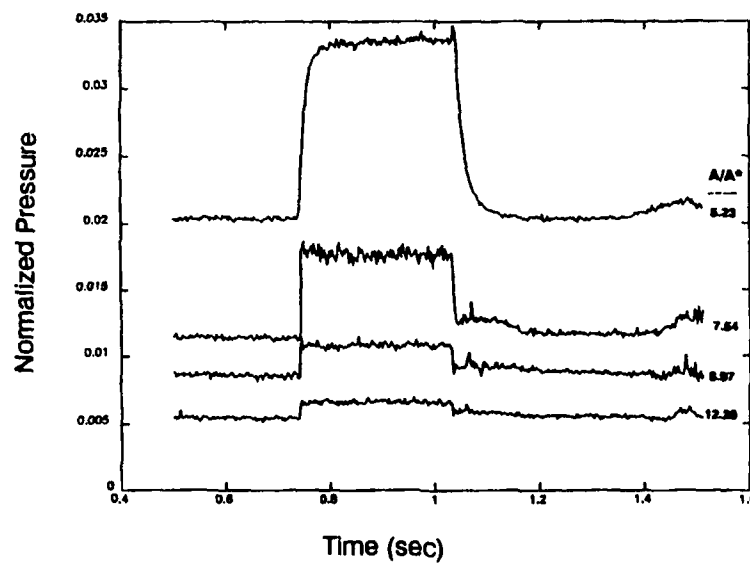
Fig. 6. Normalized Pressure Before, During, and After the Pulsed Freon Injection at Various Axial Locations (A/A*) Along the 12° Generator

24

Fig. 7. Measured Pressure Field in the Vicinity and Downstream of the Injection Port (Freon Injection)

Fig. 8. Measured Pressure Field in the Vicinity and Downstream of the Injection Port (Water Injection)

Fig. 9. Measured Pressure Field in the Vicinity and Downstream of the Injection Port (Nitrogen Injection)

Table 1. Center of Force and Total Resultant Side Force Induced on the Nozzle Wall for Different Tested Cases

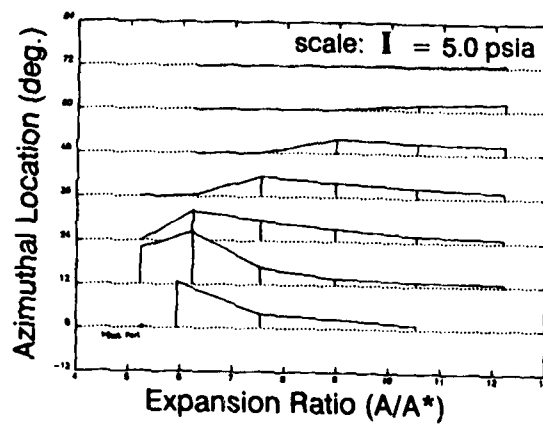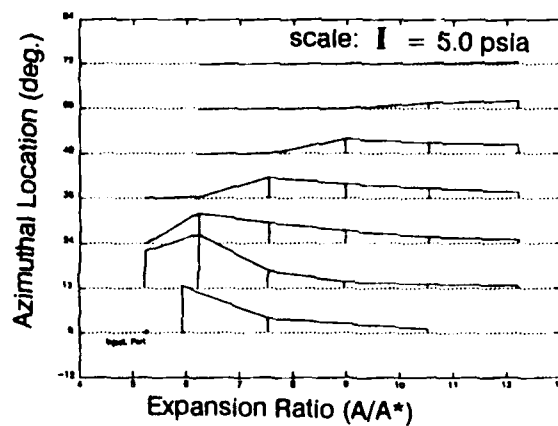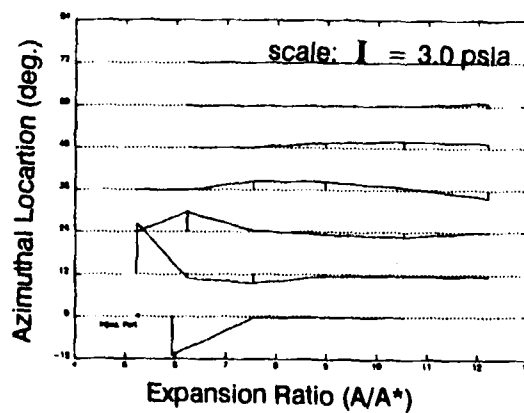|	Ratio of Mass Flow Rates Injection/Main (%)	Total Resultant Side Force (lbf)	Center of Force (in.)	Ratio of Side Force to Axial Thrust (%)
Freon-11	5.14	6.61	0.379	2.91
Freon-11	2.91	4.88	0.399	2.15
Water	3.4	6.42	0.426	2.83
Nitrogen	0.19	0.96	0	0.42
Wire (h/d = 12.5)	--	0.96	0.60	0.42
Wire (h/d = 6.25)	--	0.41	0.344	0.18

translates into 2.83% of total side force-to-axial thrust ratio, since the injection thrust force in the y-direction was calculated to be 1.042 lbf. The location of the center of force is 0.426 in. downstream from the injection port along the x-axis, which further accentuates the similarity between the two liquid injection cases (Table 1). It should be noted that the ratio of mass flow rates (injection to main flow) for the case of Freon-11 injection was 5.14%; for the case of water injection, this ratio was only 3.47%. Considering this fact and observing the similarity between the results obtained for these two cases, one concludes that results are rather insensitive to mass flow rate, and gas dynamics effects are similar for both liquid injection cases.

Compared to the liquid jet, the results obtained for the gaseous injection (nitrogen) are quite different. Figure 9 shows the pressure distribution in the vicinity and downstream of the injection port when nitrogen is being injected into the main flow. The differences between the gas and liquid injections are clearly visible by comparing Fig. 9 with Figs. 7 and 8. For one thing, the jump in pressure across the shock is not as pronounced for the nitrogen injection case. Also, there are regions where local static pressure is lower than the base pressure (local static pressure, if there were no injection). This is true, in particular, immediately downstream of the intruding jet. The discrepancies between the gas and liquid injections are expected since the gas dynamics effects are quite different. In the nitrogen injection case, a highly under-expanded, supersonic gaseous jet is being introduced into the supersonic cross-stream. Effective jet widths quickly become larger than the injectant hole, and a significant entrainment region is developed.

On the other hand, with Freon-11 or water injectants, a liquid is issued into the supersonic cross-flow. The liquid jet maintains its own shape for a longer period of time before being dispersed and evaporated, moving downstream into the main flow. The strength of the bow shock developing around the intruding jet is more pronounced in the case of liquid injection. Normal shock estimates would yield pressure jumps 10 times those reported here, but these are effective over very small areas. Thus, we estimate no greater than a 10% side force augmentation.

The results pertaining to the wire being placed in the supersonic stream, although not conclusive, are interesting. For the thinner wire where the aspect ratio (h/d) was 12.5, the total resultant side force induced on the nozzle wall is very nearly equal to that for the nitrogen injection case, while the location of center of force is considerably farther downstream of the injection port (Table 1). However, close examination of the pressure distribution in the vicinity of the wire (Fig. 10) reveals that there is a substantial difference between this case and the pressure distribution pertaining to the nitrogen injection case. Indeed, Fig. 10 indicates that the wake behind the thin wire is much smaller compared with the wake created due to injection of the under-expanded nitrogen jet. On the other hand, the pressure distribution in the vicinity of the thicker wire (h/d = 6.25) indicates the development of a rather pronounced wake (Fig. 11). The total induced side force in this case was calculated to be roughly half that for the thinner wire, while the location of center of force is moved closer to the injection port (Table 1).

As previously stated, in addition to the foregoing treatment of the accumulated data, an attempt was made to visualize the flow in the vicinity of the intruding jet by painting a thin, dark oil film on the nozzle wall. In the nitrogen injection case, the footprint of the shock could be rather easily traced, and the distance between the shock front and the injection point (standoff distance) could be observed to be 1 to 2 injection diameters. The shock track obtained by this method closely resembled the track inferred from Fig. 9 by connecting the points across which a significant jump in pressure was detected on the nozzle wall. Similar procedure was followed for the liquid injection cases (Freon-11 and water), but the shock track was not so identifiable due to the oil-washing effect of the liquids used.
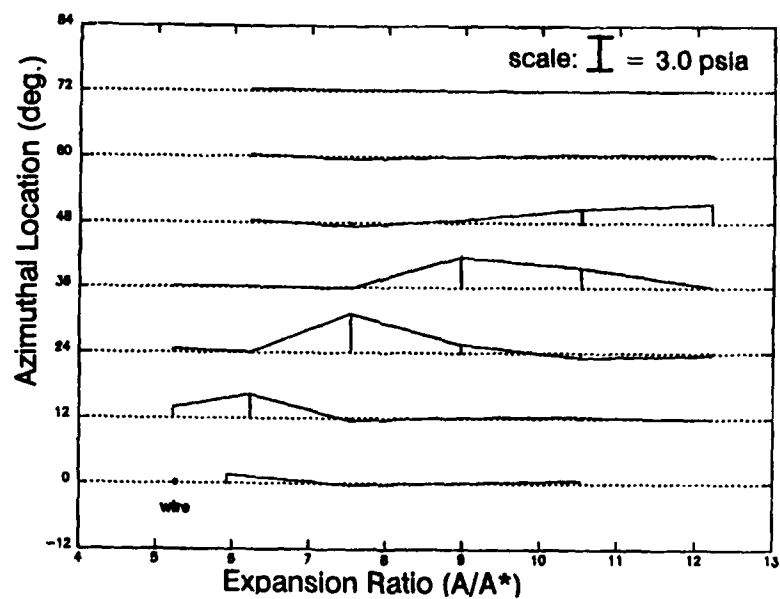
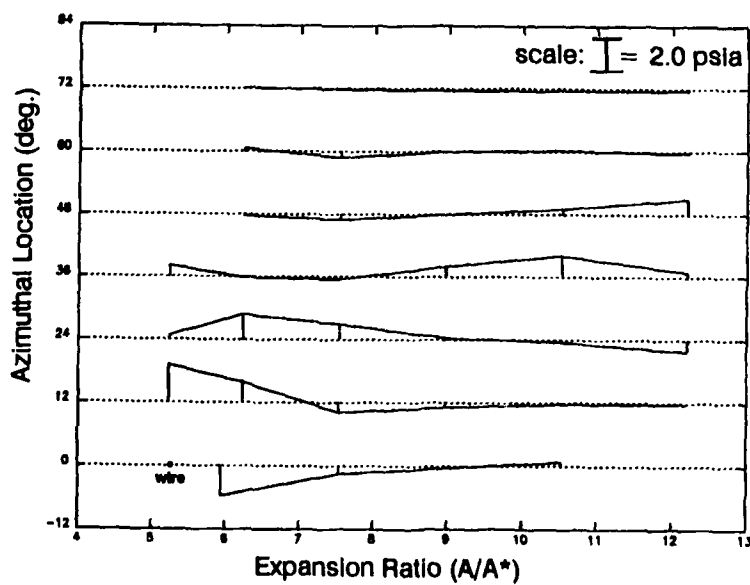Fig. 10. Measured Pressure Field in the Vicinity and Downstream of a
Wire (h/d = 12.5)

Fig. 11. Measured Pressure Field in the Vicinity and Downstream of a
Wire h/d = 6.25)

28

V. CONCLUSIONS

The results obtained for the total side force and the location of the center of force exerted on the nozzle wall due to impingement of a jet into a supersonic cross-stream for both liquid injections (Freon-11 and water) and a gas injection (nitrogen) are tabulated in Table 1. The table also includes the results for both wires (h/d = 12.5, 6.25).

The tabulated data indicate that side force-to-thrust ratios are on the order of several percent for liquid injectants. This is in excellent agreement with ratios reported from the actual flight data. The location of the center of force is determined to be approximately 0.4 in. downstream of the injection port, which corresponds to 12 in. downstream from the hole created on the nozzle wall in the actual rocket engine, when scaled. In fact, the most recent data, based on the interpreted and reduced flight data, indicates that the side force experienced by the rocket nozzle during the anomaly was nearly 8280 lbf in the y-direction. Considering that the axial thrust through each subassembly is of the order of 255,000 lbf, the side force-to-axial thrust ratio is calculated to be 3.2%. The estimation of the location of the center of force is less certain, because the precise location and the shape of the crack developed during flight cannot be pinpointed.

However, the center of force is estimated to lay somewhere within 0 to 15 in. downstream of the injection point. On the other hand, the location of the center of force obtained by integration of TVC data[27] for the solid Titan vehicles is calculated to be nearly 8 in. downstream of the injection ports.[28] Thus, the location of center of force predicted by the present investigation falls well within the expected range. Also, the compiled data presented in this report indicate that results for the liquid injectants seem to be insensitive to mass flow ratios, once sufficient fluid is injected to set up the shock interaction pattern.

It will be informative to employ other flow visualization techniques, such as schlieren or moiré deflectometry. Utilization of other gases, such as helium or SF_6, as injectants or the main flow gas will provide other valuable information, such as the effect of the gas molecular weight. Although not complete, the investigation reported here clearly demonstrates that the major cause of the side force for this flight anomaly can be solely attributed to gas dynamics effects.

29

REFERENCES

1. Callaghan, E. E., and Ruggeri, R. S., "Investigation of the Penetration of an Air Jet Directed Perpendicularly to an Air Stream," N.A.C.A. Tech. Note, No. 1615, 1948.

2. Ruggeri, R. S., Callaghan, E. E. and Bowden, D. T., "Penetration of Air Jet Issuing from Circular, Square, and Elliptical Orfices Directed Perpendicularly to an Air Stream," N.A.C.A. Tech. Note, No. 2919, 1950.

3. Callaghan, E. E., and Ruggeri, R. S., "A General Correlation of Temperature Profiles Downstream of a Heated Air Jet Directed Perpendicularly to an Air Stream," N.A.C.A. Tech. Note, No. 2466, 1951.

4. Ruggeri, R. S., "General Correlation of Temperature Profiles Downstream of a Heated Air Jet Directed at Various Angles to Air Stream," N.A.C.A. Tech. Note, No. 2855, 1952.

5. Jordinson, R., "Flow in a Jet Directed Normal to the Wind," Aero. Res. Council, R. & M., No. 3074, 1958.

6. Keffer, J. F., and Baines, W. D., "The Round Turbulent Jet in a Cross-Wind," J. Fluid Mech., Vol. 15, 1963, pp. 481-496.

7. Kamotani, V., and Gerber, I., "Experiments on a Turbulent Jet in a Cross Flow," AIAA Journal, Vol. 10, No. 11, 1972, pp. 1425-1424.

8. Chassaing, P., George, J., Claria, A., and Sananes, F., "Physical Characteristics of Subsonic Jets in a Cross-Stream," J. Fluid Mech., Vol. 62, 1974, pp. 41-64.

9. Moussa, Z. M., Trischka, J. W., and Eskinazi, S., "The Near Field in the Mixing of a Round Jet with a Cross-Stream," J. Fluid Mech., Vol. 80, 1977, pp. 49-80.

10. Holdman, J. D., and Walker, R. E., "Mixing of a Row of Jets with a Confined Crossflow," AIAA Journal, Vol. 15, No. 2, 1977, pp. 243-249.

11. Atkinson, K. N., Khan, Z. A., and Whitelaw, J. H., "Experimental Investigation of Opposed Jets Discharging Normally into a Cross-Stream," J. Fluid Mech., Vol. 115, 1982, pp. 493-504.

12. Walker, R. E., Stone, A. R., and Shander, M., "Secondary Gas Injection in a Conical Rocket Nozzle," AIAA Journal, Vol. 1, 1963, pp. 334-338.

13. Zukaski, E. E., and Spaid, F. W., "Secondary Injection of Gases into a Supersonic Flow," AIAA Journal, Vol. 2, No. 10, 1964, pp. 1689-1696.

14. Hsia, H.T.-S., Seifert, H., and Karamcheti, K., "Shock Induced by Secondary Fluid Injection," J. Spacecraft Rockets, Vol. 2, No. 1, 1965, pp. 67-72.

15. Forde, J. M., Molder, S., and Szpiro, E. J., "Secondary Liquid Injection into a Supersnic Airstream," J. Spacecraft Rockets, Vol. 3, No. 8, 1966, pp. 1172-1176.

16. Schetz, J. A., and Billig, F. S., "Penetration of Fluid Jets into a Supersonic Flow," J. Spacecraft Rockets, Vol. 3, No. 9, 1966, pp. 1658-1665.

17. Orth, R. C. and Funk, J. A., "An Experimental and Comparative Study of Jet Penetration in Supersonic Flow," AIAA Paper 67-225, 1967.

31

18. Schetz, J. A., Hawkins, P. F., and Lehman, H., "The Structure of Highly Underexpanded Transverse Jets in a Supersonic Stream," AIAA Journal, Vol. 5, 1867, pp. 882-884.

19. Kolpin, M. A., Horn, K. P., and Reichenbach, R. E., "Study of Penetration of a Liquid Injection into a Supersonic Flow," AIAA Journal, Vol. 6, No. 5, 1968, pp. 853-858.

20. Schetz, J. A., "Interaction Shock Shape for Transverse Injection in Supersonic Flow," J. Spacecraft Rockets, Vol. 7, No. 2., 1970, pp. 143-149.

21. Billig, F. S., Orth, R. C., and Lasky, M., "A Unified Analysis of Gaseous Jet Penetration," AIAA Journal, Vol. 9, 1971, pp. 1048-1058.

22. Adelberg, M., "Breakup Rate and Penetration of a Liquid Jet in a Gas Stream," AIAA Journal, Vol. 5, No. 8, 1967, pp. 1408-1415.

23. Broadwell, J. E., and Breidenthal, R. E., "Structure and Mixing of a Transverse Jet in Incompressible Flow," J. Fluid Mech., Vol. 148, 1984, pp. 405-412.

24. Less, D. M., and Schetz, J. A., "Transient Behavior of Liquid Jets Injected Normal to a High-Velocity Gas Stream," AIAA Journal, Vol. 24, No. 9, 1986, pp. 1502-1507.

25. Heister, S. D., Nguyen, T. T., and Karagozian, A. R., "Modeling of Liquid Jets Injected Transversely into a Supersonic Crossflow," AIAA Journal, Vol. 27, No. 12, 1989, pp. 1727-1734.

26. Bendat, J. S., and Piersol, A. G., "Random Data Analysis and Measurement Procedure," 2nd Ed., Wiley-Interscience Publication, 1986.

27. Cantrell, F. E., and Ervin, W. D., "Summary of Thrust Vector Control Performance of Six United Technology Center Subscale Seven-Segment Titan III-M Motors at Pressure Altitude Conditions," Report AEDC-TR-70-48, 1970.

28. Murdock, J. W., "Titan IV Leak Generated Side Force," ATM 89(4530-98)-5, The Aerospace Corporation, El Segundo, CA, 1989.

LABORATORY OPERATIONS

The Aerospace Corporation functions as an "architect-engineer" for national security projects, specializing in advanced military space systems. Providing research support, the corporation's Laboratory Operations conducts experimental and theoretical investigations that focus on the application of scientific and technical advances to such systems. Vital to the success of these investigations is the technical staff's wide-ranging expertise and its ability to stay current with new developments. This expertise is enhanced by a research program aimed at dealing with the many problems associated with rapidly evolving space systems. Contributing their capabilities to the research effort are these individual laboratories:

Aerophysics Laboratory: Launch vehicle and reentry fluid mechanics, heat transfer and flight dynamics; chemical and electric propulsion, propellant chemistry, chemical dynamics, environmental chemistry, trace detection; spacecraft structural mechanics, contamination, thermal and structural control; high temperature thermomechanics, gas kinetics and radiation; cw and pulsed chemical and excimer laser development, including chemical kinetics, spectroscopy, optical resonators, beam control, atmospheric propagation, laser effects and countermeasures.

Chemistry and Physics Laboratory: Atmospheric chemical reactions, atmospheric optics, light scattering, state-specific chemical reactions and radiative signatures of missile plumes, sensor out-of-field-of-view rejection, applied laser spectroscopy, laser chemistry, laser optoelectronics, solar cell physics, battery electrochemistry, space vacuum and radiation effects on materials, lubrication and surface phenomena, thermionic emission, photosensitive materials and detectors, atomic frequency standards, and environmental chemistry.

Electronics Research Laboratory: Microelectronics, solid-state device physics, compound semiconductors, radiation hardening; electro-optics, quantum electronics, solid-state lasers, optical propagation and communications; microwave semiconductor devices, microwave/millimeter wave measurements, diagnostics and radiometry, microwave/millimeter wave thermionic devices; atomic time and frequency standards; antennas, rf systems, electromagnetic propagation phenomena, space communication systems.

Materials Sciences Laboratory: Development of new materials: metals, alloys, ceramics, polymers and their composites, and new forms of carbon; nondestructive evaluation, component failure analysis and reliability; fracture mechanics and stress corrosion; analysis and evaluation of materials at cryogenic and elevated temperatures as well as in space and enemy-induced environments.

Space Sciences Laboratory: Magnetospheric, auroral and cosmic ray physics, wave-particle interactions, magnetospheric plasma waves; atmospheric and ionospheric physics, density and composition of the upper atmosphere, remote sensing using atmospheric radiation; solar physics, infrared astronomy, infrared signature analysis; effects of solar activity, magnetic storms and nuclear explosions on the earth's atmosphere, ionosphere and magnetosphere; effects of electromagnetic and particulate radiations on space systems; space instrumentation.